

Separating double-beta decay events from solar neutrino interactions in kiloton-scale liquid scintillator detectors

Andrey Elagin^{a,*}, Henry J. Frisch^a, Jonathan Ouellet^b, Lindley Winslow^b

^a *Enrico Fermi Institute, University of Chicago, Chicago, IL, 60637*

^b *Massachusetts Institute of Technology, Cambridge, MA 02139*

Abstract

We propose a technique for separating $0\nu\beta\beta$ -decay events from background due to ${}^8\text{B}$ solar neutrino interactions in a liquid scintillator detector. The technique compares event topology of the signal and background events using spherical harmonics analysis of the early light emitted in $0\nu\beta\beta$ -decay and ${}^8\text{B}$ events. Selection of early photons using fast photo-detectors allows for separation of directional Cherenkov from isotropic scintillation light and identification of two event topologies based on the spatial distribution of the early photons in the detector.

*Corresponding Author: elagin@hep.uchicago.edu

7 **Contents**

8	1 Introduction	3
9	2 Detector Model	5
10	3 Event Topology and Spherical Harmonics Analysis	8
11	3.1 Topology of $0\nu\beta\beta$ -decay and 8B Events	8
12	3.2 Description of Spherical Harmonics Analysis	9
13	3.3 Spherical Harmonics Analysis and Off-center Events	12
14	3.4 Implementation of the spherical harmonics analysis	12
15	4 Performance and Experimental Challenges	16
16	4.1 Performance of the spherical harmonics analysis on $0\nu\beta\beta$ decay and 8B events.	16
17	4.2 Experimental challenges	17
18	5 Conclusions	21
19	A $0\nu\beta\beta$ decay vs ${}^{10}C$ background	22

1. Introduction

Over the past decade, neutrino oscillation experiments have conclusively established that neutrinos have mass. However, one of the most fundamental and still open questions in particle physics is the nature of that mass. Is the neutrino unique in the Standard Model with a Majorana type mass, as is predicted by most theoretical arguments, or does it have a Dirac type mass, like the rest of the fermions in the Standard Model? A Majorana mass would have far reaching implications, from explaining the lightness of the neutrino and providing a bridge to higher energy phenomena through the see-saw mechanism [CITATION] to providing the required lepton-number violation (LNV) and CP-violation needed for leptogenesis to explain the baryon asymmetry of the universe [?]. Conversely, a Dirac neutrino could point to an underlying symmetry of the Universe. Presently, the most promising technique for answering these questions is the search for Neutrinoless Double-Beta ($0\nu\beta\beta$) decay [CITATION]. In this decay, a nucleus undergoes a second order β -decay without producing any neutrinos, $(Z, A) \rightarrow (Z + 2, A) + 2\beta^-$. The resulting decay products are ejected with a total kinetic energy equal to the decay Q -value, and most of this is carried by the electrons which have typical kinetic energies of $\sim 1\text{--}2$ MeV.

The standard mechanism of $0\nu\beta\beta$ decay is parameterized by the *effective Majorana mass*, $m_{\beta\beta} \equiv \left| \sum_i U_{ei}^2 m_i \right|$, where U_{ei} are the elements of the PMNS matrix and m_i are the neutrino masses [CITATION]. Recently, this search has generated a significant amount of experimental interest, with current experiments searching for $0\nu\beta\beta$ decay of ^{76}Ge [?], ^{130}Te [?] and ^{136}Xe [? ?]. At present, $0\nu\beta\beta$ decay has never been convincingly observed, but limits place the half-lives at longer than $10^{23}\text{--}10^{25}$ yr in the isotopes studied. These limits translate to a limit on $m_{\beta\beta} \lesssim 150\text{--}700$ meV, with the majority of the spread on this limit coming from uncertainty in the nuclear modeling. The next generation of $0\nu\beta\beta$ decay experiments seek to be sensitive enough to detect or rule out $0\nu\beta\beta$ decay down to $m_{\beta\beta} < 10$ meV. This will require, among other things, \sim a ton of active isotope, a good energy resolution, and a near zero background in the region of interest (ROI) [CITATION?].

Over the past few years, liquid scintillator-based detectors have proven to be a competitive technology in this search [CITATION?]. Their primary advantage is in their scalability to larger active masses, which entails dissolving larger amounts of active isotope into the liquid scintillator (LS). This feature allows for rapid scaling to the 1 ton or more of active isotope. In a large LS detector, where backgrounds from the outside of the detector can be efficiently self-shielded or tagged and vetoed, the two backgrounds relevant to $0\nu\beta\beta$ decay are $2\nu\beta\beta$ and electron scattering (ES) interactions of ^8B solar neutrinos.

Two neutrino double beta ($2\nu\beta\beta$) decay is the Standard Model allowed second order β -decay channel where lepton number is conserved, $(Z, A) \rightarrow (Z, A + 2) + 2\beta + 2\bar{\nu}_e$. Since the kinetic energy of the neutrinos is practically never detected, the resulting $2\nu\beta\beta$ spectrum is broadened from 0 MeV up to the decay Q -value. The high energy tail of this spectrum forms a background for the $0\nu\beta\beta$ signal. Since it is intrinsic to the target isotope and the decay kinematics are nearly identical to $0\nu\beta\beta$ decay, $2\nu\beta\beta$ can only be separated from $0\nu\beta\beta$ with a detector with powerful enough resolution (see Fig. 1). Present LS-based detectors achieve typical energy resolutions of $\sigma(E) \sim 5\% / \sqrt{E(\text{MeV})}$. The next

generation of detectors will improve up this... Something about photo-coverage (etc). Eventually this will fold back in the question of slowing down the scintillation signal and improving the Cherenkov signal at the cost of decreasing the total light yield.

The spectrum of ES interactions of ^8B solar neutrinos falls slowly over the range 2–3 MeV, creating a nearly flat background across the $0\nu\beta\beta$ ROI. However, these interactions produce only a single ~ 2.5 MeV electron, rather than two ~ 1.2 MeV electrons as in $0\nu\beta\beta$. In a LS, this difference in event topology manifests as two distinct distributions of Cherenkov photons, and thus creates a way to tag and remove these ^8B solar neutrino events. As we have shown in previous works, photo-detectors with timing resolution of ~ 100 ps can resolve the prompt Cherenkov photons from the slower scintillation signal [?]. The challenge is that for a given event, we expect XXX Cherenkov photons with which to reconstruct the event topology.

In this paper, we proposed to use a spherical harmonic decomposition to analyze the distribution of early photo-electrons (PE) to discriminate between ^8B solar neutrinos and $0\nu\beta\beta$ decay events. In Section 2, we describe the detector model we will use throughout this paper. In Section ??, we introduce the spherical harmonic decomposition, and discuss the performance of this analysis in Section 4.

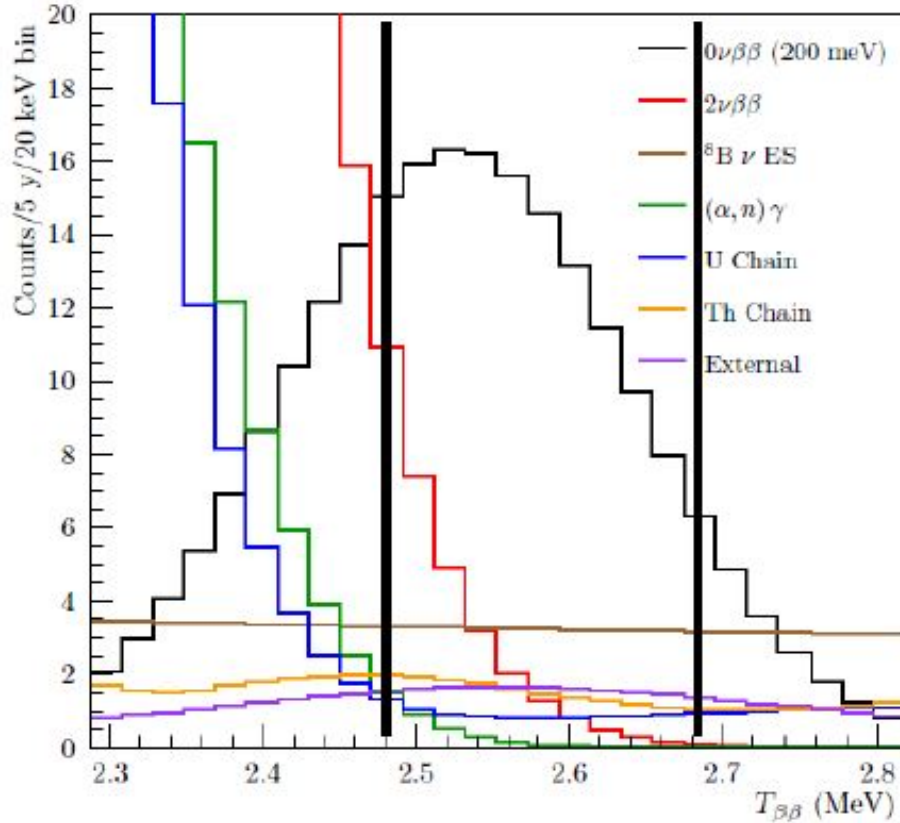


Figure 1: SNO+ Phase I signal and background energy spectrum (visible kinetic energy reconstructed under a $0\nu\beta\beta$ hypothesis). Plot taken from [?]

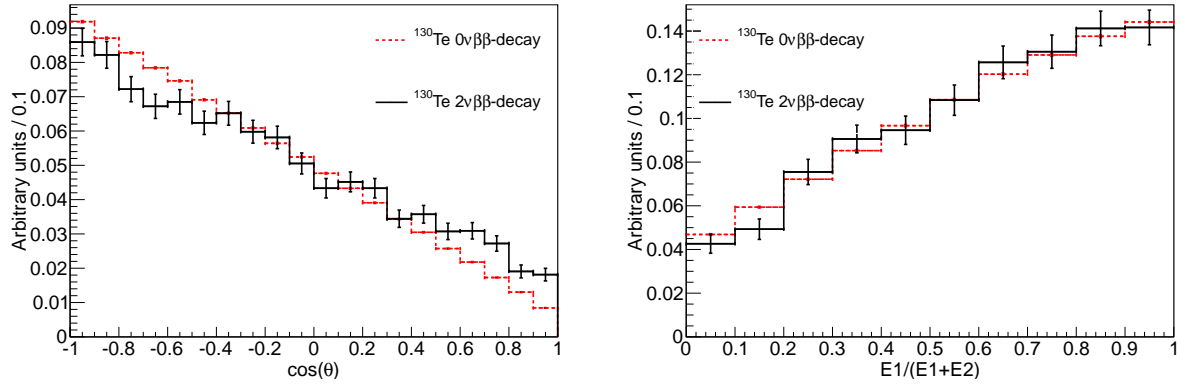


Figure 2: Comparison between kinematics of $0\nu\beta\beta$ (dashed red lines) and $2\nu\beta\beta$ decays (solid black lines) for events with the total kinetic energy of the electrons above 90% of the Q-value. *Left:* Cosine of the angle between two electrons. *Right:* Fraction of energy carried by one of the two electrons. Due to limited statistic around the energy spectrum end point for $2\nu\beta\beta$ decay we show statistical errors for each bin.

2. Detector Model

Copy info from [?]:

In order to study the effects relevant to directional reconstruction in liquid scintillators, a Geant4[? ?] simulation has been constructed. The simulation uses Geant4 version 4.9.6 with the default liquid scintillator optical model, in which optical photons are assigned the group velocity in the wavelength region of normal dispersion.

The detector geometry is a sphere of 6.5 m radius filled with scintillator. Figure ?? shows the geometry and the Cherenkov light from an example ^{116}Cd $0\nu\beta\beta$ event. The default scintillator properties have been chosen to match a KamLAND-like scintillator[?]: 80% n-dodecane, 20% pseudocumene and 1.52 g/l PPO. The scintillator properties implemented in the simulation include the atomic composition and density ($\rho = 0.78$ g/ml), the wavelength-dependent attenuation length[?] and refractive index[?], the scintillation emission spectrum[?], emission rise time ($\tau_r = 1.0$ ns) and emission decay time constants ($\tau_{d1} = 6.9$ ns and $\tau_{d2} = 8.8$ ns with relative weights of 0.87 and 0.13)[?], scintillator light yield (9030 photons/MeV), and the Birks constant ($kB \approx 0.1$ mm/MeV)[?]. This is a standard scintillator. The attenuation length at 400 nm, the position of the peak standard bialkali photocathode efficiency, is 25 m. The attenuation length drops precipitously between 370 nm and 360 nm from 6.5 m to 0.65 m. We use this drop to define the cutoff wavelength at 370 nm. Variations from the baseline KamLAND case are discussed below.

Re-emission of absorbed photons in the scintillator bulk volume and optical scattering, specifically Rayleigh scattering, have not yet been included by default. A test simulation shows that the effect of optical scattering is negligible [?].

The inner sphere surface is used as the photodetector. It is treated as fully absorbing (no reflections), with a photodetector coverage of 100%. As in the case of optical scattering, reflections at the sphere are a small effect that would create a small tail at longer times. Two important photodetector properties have been varied: 1) the transit-time spread (TTS, default $\sigma = 0.1$ ns) and 2) the wavelength-dependent quantum efficiency (QE) for photoelectron

production. The default is the QE of a bialkali photocathode (Hamamatsu R7081 PMT)[?]. The QE values as a function of wavelength come from the Double Chooz[?] Monte Carlo simulation. We note that the KamLAND 17-inch PMTs use the same photocathode type with similar quantum efficiency. We are neglecting any threshold effects in the photodetector readout electronics.

Four effects primarily contribute to the timing of the scintillator detector system: the travel time of the particle, the time constants of the scintillation process, chromatic dispersion, and the timing of the photodetector.

In the energy range important for $0\nu\beta\beta$, a 1.4 MeV electron travels a total path length of 0.8 cm, has a distance from the origin of 0.6 cm in 0.030 ± 0.004 ns and takes 0.028 ± 0.004 ns to drop below Cherenkov threshold. We note that due to scattering the final direction of the electron before it stops does not correspond to the initial direction; however the scattering angle is small while the majority of Cherenkov light is produced. The Cherenkov light thus encodes the direction of the primary electron. The scattering physics is handled by Geant4's "Multiple Scattering" process which is valid down to 1 keV, where atomic shell structure becomes important[?].

The scintillator-specific rise and decay times are the second effect that determines the timing in a scintillator detector. The first step in the scintillation process is the transfer of energy from the solvent to the solute. The time constant of this energy transfer accounts for a rise time in scintillation light emission. Past neutrino experiments were not highly sensitive to the effect of the scintillation rise time, which is the reason why there is a lack of accurate numbers. We assume a rise time of 1.0 ns; more detailed studies are needed in the future. The two time constants used to describe the falling edge of the scintillator emission time distribution (quoted above) are values specific to the KamLAND scintillator.

Chromatic dispersion is the third effect that determines the timing in a scintillator detector. Due to the wavelength-dependence of the refractive index the speed of light in the scintillator (see Equation (??)) increases with increasing photon wavelengths for normal dispersion, with red light traveling faster than blue light.

Photoelectrons coming from Cherenkov light are on average created about 0.5 ns earlier than PEs from scintillation light. The RMS values from PE time distributions for Cherenkov and scintillation light are both about 0.5 ns. Note that these numbers include the effect of the finite electron travel time.

The fourth effect determining the timing in a scintillator detector is the timing of the photodetectors. The measurement of the arrival times of single photoelectrons is affected by the transit-time spread (TTS) of the photodetectors, a number which can be different by orders of magnitude depending on the detector type. The default TTS of 0.1 ns (σ) can be achieved with large area picosecond photodetectors (LAPPDs)[? ? ?] and possibly hybrid photodetectors (HPDs)[?]; even significantly lower TTS numbers are realistic with the LAPPD[? ? ?].

The primary quantities provided by the Geant4 simulation are the photoelectron hit positions and the detection times after the TTS resolution has been applied. In section ?? these quantities are then used for event reconstruction.

Figures 3 and 4 show simulation output relevant for further discussion.

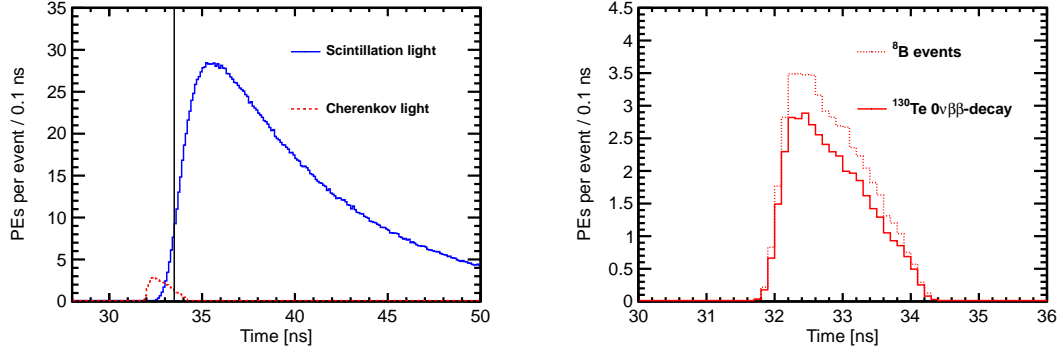


Figure 3: *Left*: Photo-electron (PE) arrival times after application of the photo-detector transit time spread (TTS) of 100 ps for the simulation of 1000 $0\nu\beta\beta$ decay events of ^{130}Te at the center of the detector. PEs from Cherenkov light (*dashed red line*) and scintillation light (*solid blue line*) are compared. The black vertical line illustrates a time cut at 33.5 ns. *Right*: Comparison between Cherenkov PE arrival time for ^{130}Te $0\nu\beta\beta$ decay (*solid line*) and ^8B (*dotted line*) events. **Distributions of the scintillation PEs arrival time are indistinguishable between ^{130}Te $0\nu\beta\beta$ decay and ^8B due to identical total energy in the event, $Q(^{130}\text{Te}) = 2.526$ MeV.**

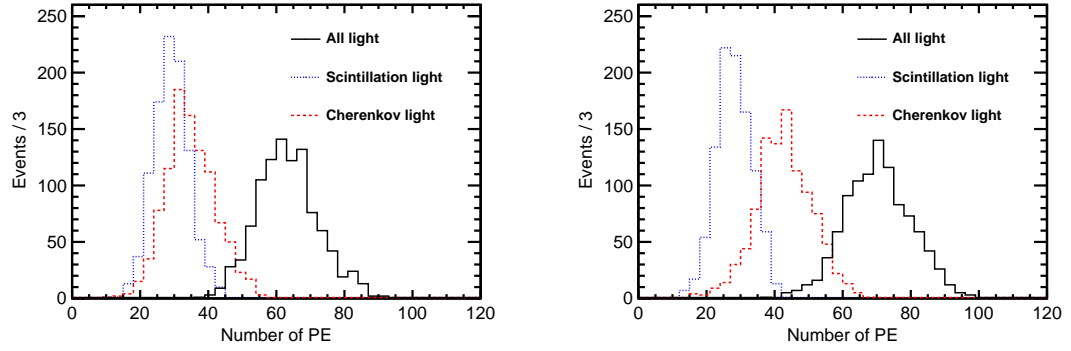


Figure 4: Number of Cherenkov (*dashed red line*), scintillation (*dotted blue line*), and total (*solid black line*) PEs for the simulation of 1000 ^{130}Te $0\nu\beta\beta$ decay (*left panel*) and ^8B (*right panel*) events.

3. Event Topology and Spherical Harmonics Analysis

3.1. Topology of $0\nu\beta\beta$ -decay and 8B Events

Electrons in the energy range around Q-value of all isotopes considered for $0\nu\beta\beta$ -decay searches are above Cherenkov threshold in liquid scintillators. Each electron above the threshold will produce a fuzzy ring of Cherenkov light at the detector surface. The fuzziness of the ring depends on electron scattering. In most cases Cherenkov rings from low energy electrons degrade to randomly shaped clusters of Cherenkov photons around direction of the electron track.

Large fraction of $0\nu\beta\beta$ -decay events will have two Cherenkov clusters¹ as opposed to one cluster from 8B events. Therefore separation of $0\nu\beta\beta$ -decay signal from 8B background depends on ability to identify topology of the Cherenkov light on the detector sphere on top of uniformly distributed scintillation light. We show that analysis of spherical harmonics of the early photons allows to achieve noticeable separation between $0\nu\beta\beta$ -decay and 8B events.

In order to illustrate differences between different event topologies we introduce three event topologies: two electrons produced back-to-back at 180° angle, two electrons at 90° angle, and a single electron. The two former are representative topologies of $0\nu\beta\beta$ -decay signal events and the latter represents 8B background events. Figure 5 shows Cherenkov photon distributions of 5 MeV electrons for each of the three topology. Overlay of 100 events with no QE applied is shown in order to make Cherenkov rings visible.

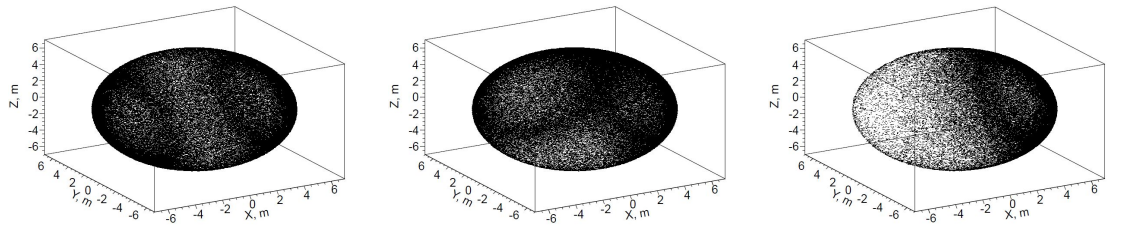


Figure 5: Cherenkov photons distributions on the detector sphere for the three representative event topologies: two back-to-back electrons (*left*), two electrons at 90° angle (*middle*), and a single electron (*center*). All electrons are 5 MeV and originate at the center of the detector. 100 events overlaid for better visibility of the Cherenkov rings. 100% QE is assumed. **These can not be included as PDFs, but my conversion shrunk the size.**

In practice Cherenkov rings from low energy electrons are not clearly visible. Cherenkov clusters that form at lower energies are shown in Fig. 6. All Cherenkov photons produced in a single event are shown for the three event topologies with total kinetic energy of 2.529 MeV that corresponds to Q-value of ${}^{130}\text{Te}$. One can try to guess the event topology by comparing different segments of the detector sphere.

More realistic examples of ${}^{130}\text{Te}$ $0\nu\beta\beta$ -decay and 8B events simulated at the center of the detector are shown in Fig. 7. Early PEs from Cherenkov and scintillation light are shown. Default simulation QE is applied. Time cut of 33.5 ns on the photon arrival time is used to select early PEs. Uniformly distributed scintillation light make it

¹Only one Cherenkov cluster is produced when either the angle between the two $0\nu\beta\beta$ -decay electrons is too small or when the energy splits between the electrons in such a way that one electron falls below the Cherenkov threshold.

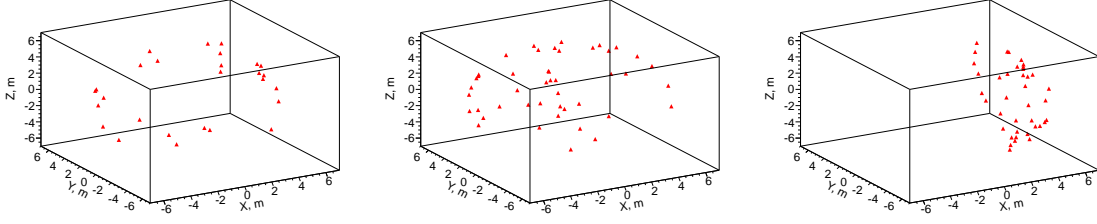


Figure 6: Cherenkov photons distributions on the detector sphere for the three representative event topologies: two back-to-back 1.26 MeV electrons (*left*), two 1.26 MeV electrons at 90° angle (*middle*), and a single 2.529 MeV electron (*center*). All electrons originate at the center of the detector. One randomly selected event is chosen for each category. Default QE is applied.

more difficult to guess the event topology. Nevertheless we show that there is still sufficient difference in the spatial distribution of the early PEs to separate two track and single track events.

For quantitative description of the difference in the event topology we analyze spherical harmonics of the photon distributions on the detector sphere. We construct rotation invariant variables and compare them between signal and background events. As it is shown in the bottom part of Fig. 7 $0\nu\beta\beta$ -decay become indistinguishable from single track topology when the angle between two electrons is small (two degenerate tracks). Event topologies of $0\nu\beta\beta$ -decay and 8B events are also very similar when only one electron from $0\nu\beta\beta$ -decay is above the Cherenkov threshold. Therefore spherical harmonics analysis is most efficient for events with large angular separation between the two electrons and when both electrons are above Cherenkov threshold.

In this paper we focus on topological difference between two tracks and single track events and do not make any attempt to use absolute directional information to suppress single track events where direction of the track is consistent with the direction of solar neutrinos. Once a single track topology is established one can use a centroid method (see Ref. [?]) to reconstruct directionality of the track (or two degenerate tracks) and suppress events that are aligned with the direction of 8B solar neutrinos.

3.2. Description of Spherical Harmonics Analysis

A function $f(\theta, \phi)$ can be decomposed to a sum of spherical harmonics:

$$f(\theta, \phi) = \sum_{l=0}^{\infty} \sum_{m=-l}^l f_{lm} Y_{lm}(\theta, \phi), \quad (1)$$

where Y_{lm} are Laplace's spherical harmonics defined in real-value basis using Legendre polynomials P_l :

$$Y_{lm} = \begin{cases} \sqrt{2} N_{lm} P_l^m(\cos\theta) \cos m\phi, & \text{if } m > 0 \\ N_{lm} = \sqrt{\frac{(2l+1)}{4\pi} \frac{(l-m)!}{(l+m)!}}, & \text{if } m = 0 \\ \sqrt{2} N_{l|m|} P_l^{|m|}(\cos\theta) \sin |m|\phi, & \text{if } m < 0 \end{cases} \quad (2)$$

Coefficients f_{lm} are defined as

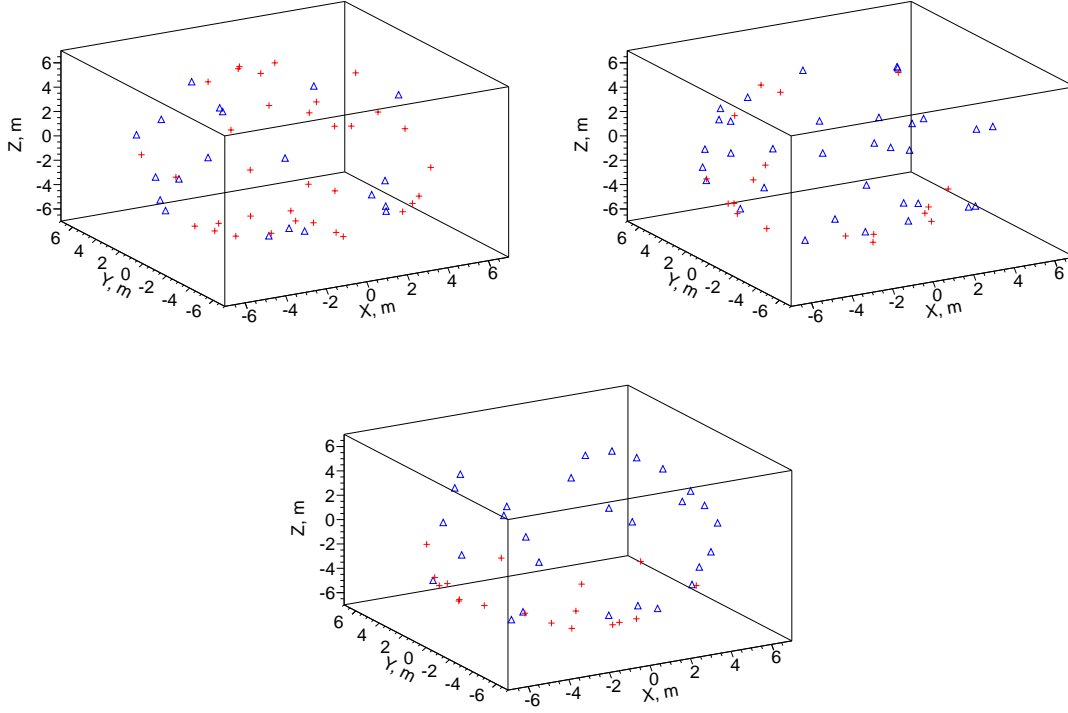


Figure 7: Examples of PEs position on the detector sphere after time cut of 33.5ns. PEs from Cherenkov (red) and scintillation light (blue) are compared. *Top left:* ^{130}Te $0\nu\beta\beta$ decay back-to-back electrons: $E_1=1.257$ MeV, $E_2=1.270$ MeV, $\cos(\theta)=-0.908$. *Top right:* ^{130}Te $0\nu\beta\beta$ decay electrons at $\sim 90^\circ$: $E_1=1.264$ MeV, $E_2=1.263$ MeV, $\cos(\theta)=-0.029$. *Bottom left:* ^{130}Te $0\nu\beta\beta$ decay electrons at $\sim 0^\circ$: $E_1=1.186$ MeV, $E_2=1.340$ MeV, $\cos(\theta)=0.888$. *Bottom right:* 2.529 MeV single electron. Events are simulated at the center of the detector. Default QE is applied.

$$f_{lm} = \int_0^{2\pi} d\phi \int_0^\pi d\theta \sin\theta f(\theta, \phi) Y_{lm}(\theta, \phi) \quad (3)$$

Equation 4 defines power spectrum of $f(\theta, \phi)$ in spherical harmonics representation, s_l , where l is a multiple moment. The power spectrum s_l is invariant under rotation. It is unique to each of the functions $f_i(\theta, \phi)$, $i = 1, 2, 3, \dots$, that can not be transformed into each other by rotation.

$$s_l = \sum_{m=-l}^{m=l} |f_{lm}|^2 \quad (4)$$

One can consider PEs distribution for each of $0\nu\beta\beta$ -decay signal or background event as a function $f_i(\theta, \phi)$. Events with similar power spectrum would correspond to PE distributions on the detector sphere that can be closely aligned by a rotation. Such PE distributions belong to events with similar topology.

Topology of $0\nu\beta\beta$ -decay signal or background in a spherical detector determines the distribution of the PE's on the detector sphere and therefore a set of s_l 's can serve as a quantitative figure of merit for different event topologies.

Rotation invariance of s_l 's ensures that this figure of merit does not depend on the orientation of the event with respect to the chosen coordinate frame.

Sum of s_l 's over all multiple moments equals to L2 norm of the function $f(\theta, \phi)$:

$$\sum_{l=0}^{\infty} s_l = \int_{\Omega} |f(\theta, \phi)|^2 d\Omega. \quad (5)$$

Therefore normalized power spectrum

$$S_l = \frac{s_l}{\sum_{l=0}^{\infty} s_l} = \frac{s_l}{\int_{\Omega} |f(\theta, \phi)|^2 d\Omega} \quad (6)$$

can be used to compare shapes of various functions $f(\theta, \phi)$ with different normalization. The total number of PEs detected on the detector sphere fluctuates from event to event, therefore in all of the following we use normalized power S_l .

Figure 8 compares normalized power spectrum for the three representative event topologies that have been already shown in Fig. 5. We note that most of the information contains in the power spectrum with $l < 6$. In most cases we found that there is no need to calculate S_l for $l > 3$ to achieve maximal separation between $0\nu\beta\beta$ -decay and 8B events, because fluctuations in the PE distribution produce a lot of noise in the power spectrum for higher orders of multiple moments.

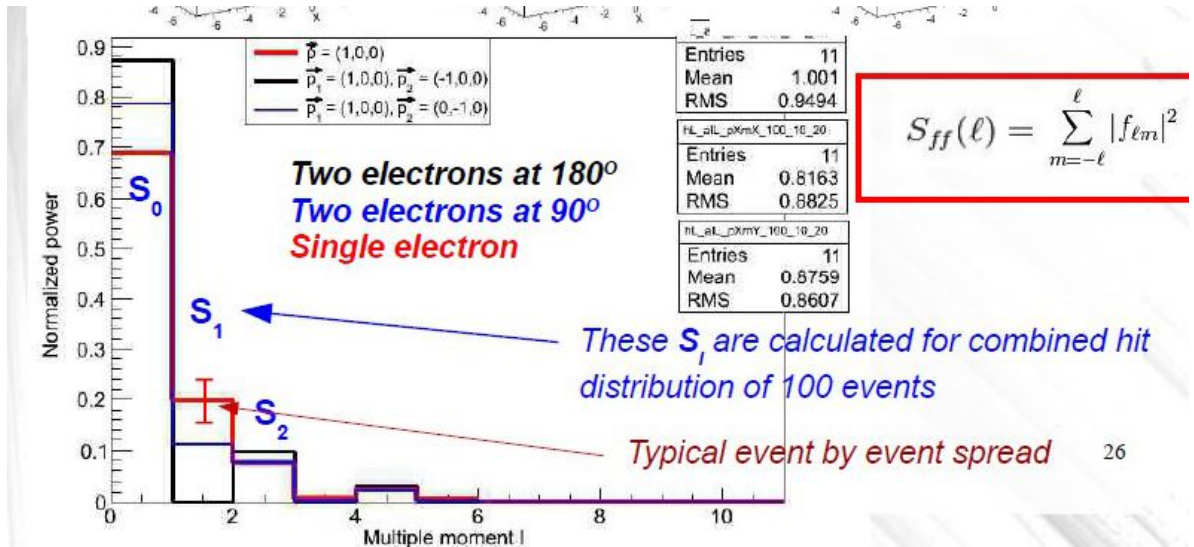


Figure 8: Average S_l values for two electrons at 180 degree (color1) and 90 degree (color2) 1.5 MeV each and a single electron (color3) with the energy of 3 MeV. Error bars are RMS values of each corresponding individual S_l distribution (each consists of 1000 events simulated at the center of the detector) indicating typical event-by-event variation.

3.3. Spherical Harmonics Analysis and Off-center Events

In order to compare spherical harmonics for events with vertices located off-center anywhere inside the detector volume a coordinate transformation for each photon hit is needed. The necessary transformation applied for each PE within an event is illustrated in Fig. 9. Solid circle with radius R schematically shows actual detector boundaries. Dotted circle shows a new sphere with the same radius R , which now has the event vertex in its center. The radius vector of each PE is stretched or shortened to its intersection with this new sphere using transformation $\vec{r}_{PE}' = \frac{\vec{a}}{|\vec{a}|} \cdot R$. Where \vec{r}_{PE}' is a new radius vector of a PE and $\vec{a} = \vec{r}_{PE} - \vec{r}_{vtx}$ with \vec{r}_{PE} and \vec{r}_{vtx} being radius vectors of the PE and the vertex in the original coordinates respectively.

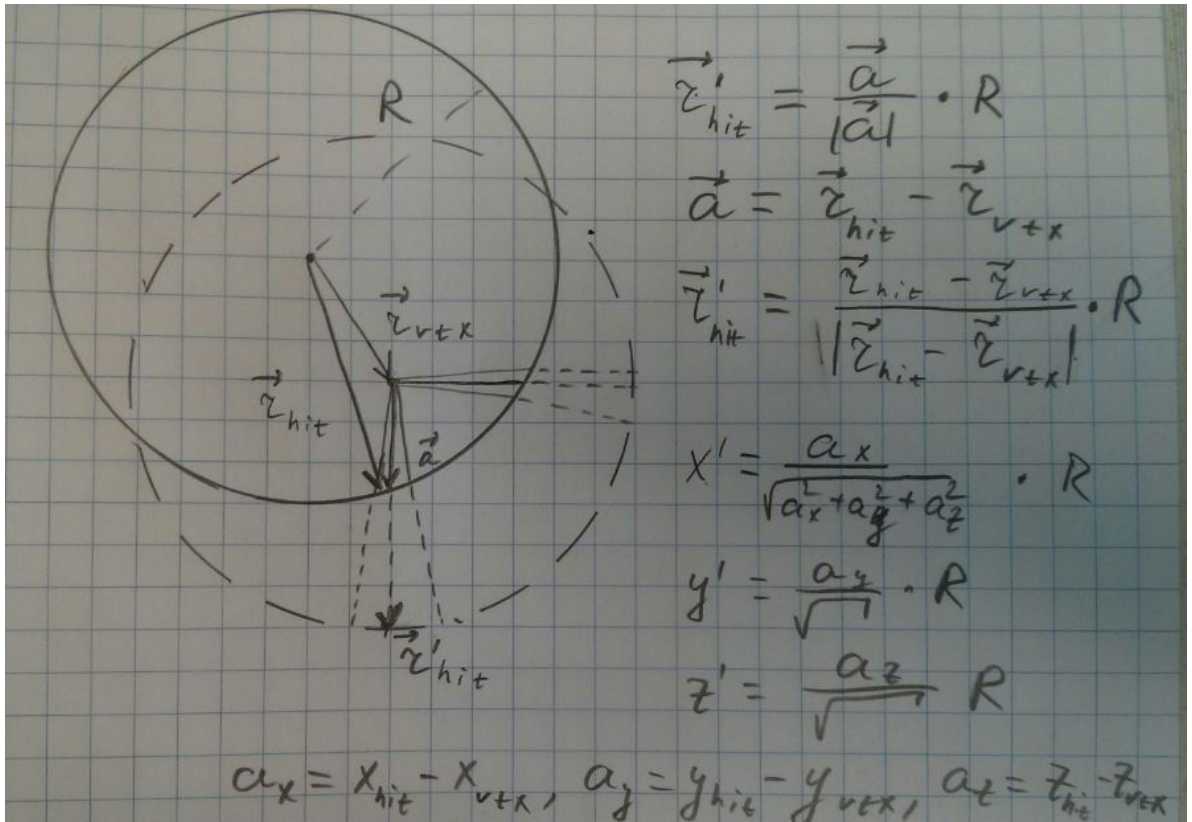


Figure 9: Coordinate transformation applied to events that are off-center. Solid circle schematically shows actual detector boundaries. Dotted circle shows a new sphere of radius $R=6.5$ m with the event vertex position in the center. The radius vector of each photon hit is stretched or shortened until intersection with this new sphere using transformation $\vec{r}_{hit}' = \frac{\vec{a}}{|\vec{a}|} \cdot R$. Where \vec{r}_{hit}' is a new radius vector of the photon hit, R is detector sphere radius, and $\vec{a} = \vec{r}_{hit} - \vec{r}_{vtx}$ with \vec{r}_{hit} and \vec{r}_{vtx} being radius vectors of the photon hit and vertex position in original coordinates and correspondingly.

3.4. Implementation of the spherical harmonics analysis

For each event we create a 2-D histogram, θ vs ϕ , with the distribution of PEs on the detector surface. We then treat this histogram as a function $f(\theta, \phi)$ where the value of the function for any pair of θ and ϕ is equal to the number of PE in the histogram bin corresponding to that pair.

202 Coefficients f_{lm} from Eq. 3 are calculated using a Monte Carlo integration technique. Variables S_0 , S_1 , S_2 , and S_3
203 are calculated using Eqs.4 - 6.

204 To illustrate spherical harmonics analysis technique we compare distributions of S_0 , S_1 , S_2 , and S_3 for the three
205 representative event topologies described in Sec. 3.1. Almost all the information about event topology is carried by
206 Cherenkov light. Therefore we first show spherical harmonics for back-to-back, 90° and single track topologies based
207 on Cherenkov PEs only (see Fig. 10).

208 Two top panels of Fig. 10 show 2-dimensional distributions, S_0 vs S_1 and S_2 vs S_3 , to demonstrate that all four
209 S_l 's provide separation between event topologies. No QE is applied in simulation of these events. We also introduce
210 a 1-dimensional variable, S_{01} (bottom panel of Fig. 10), that has the best separation power for majority of event
211 topologies considered in this paper. S_{01} is defined as a projection of S_1 vs S_2 distribution onto a linear fit of this 2-D
212 distribution.

213 The effects due to presence of scintillation light and applying default QE are shown in Fig. 11. Spherical harmonics
214 of the same three representative event topologies are now calculated using early light (photons with arrival time
215 less than 33.5 ns) that contains both directional Cherenkov light and uniform scintillation light. Default QE is also
216 applied. Higher order multiple moments, S_2 and S_3 , no longer provide noticeable separation between different event
217 topologies.

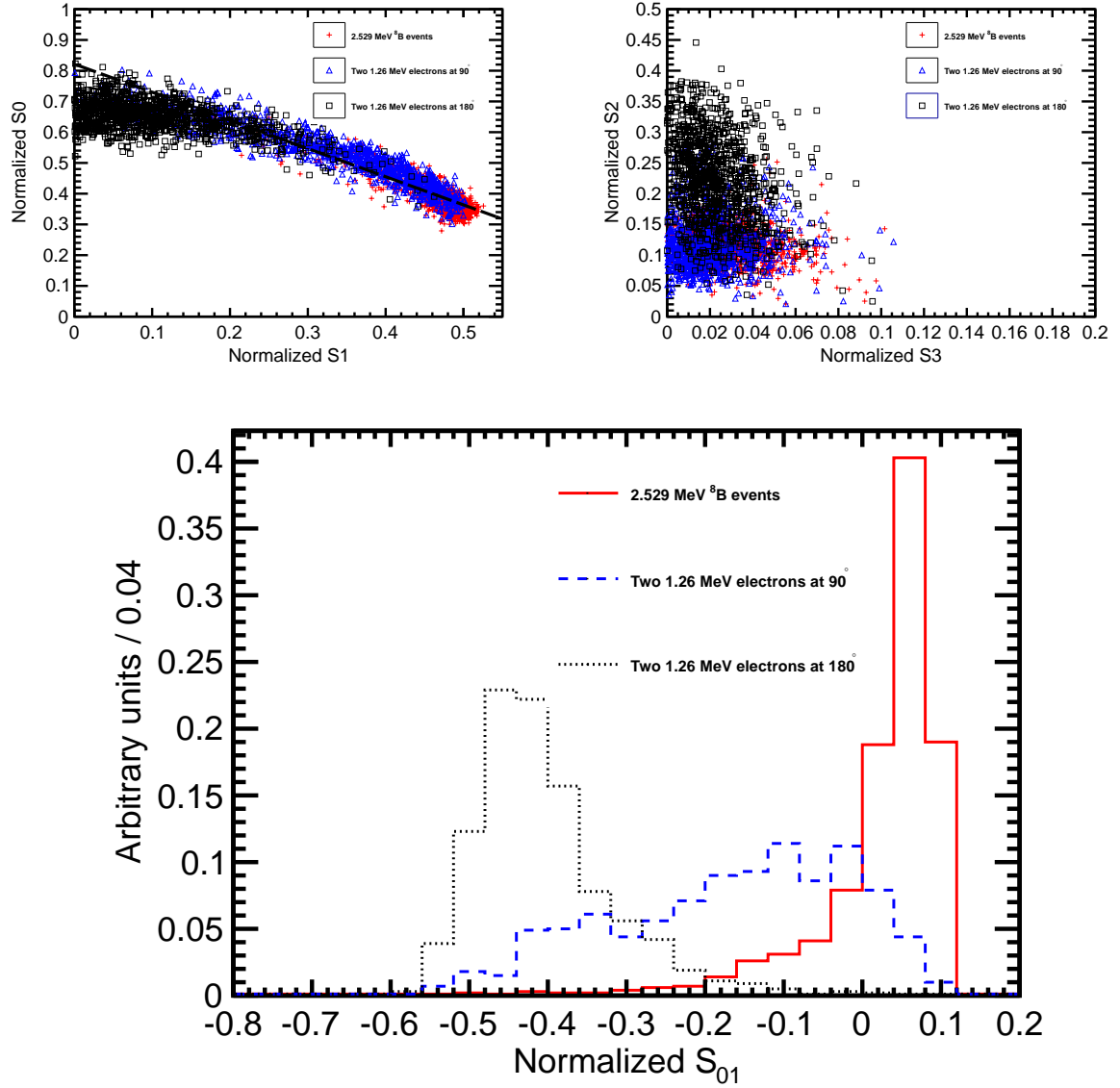


Figure 10: Spherical harmonics for three event topologies: two back-to-back 1.26 MeV electrons (black squares and black dotted line), two 1.26 MeV electrons at 90° angle (blue triangles and blue dashed line), and a single 2.529 MeV electron representing ^8B background (red crosses and red solid line). Simulation of 1000 events originated at the center of the sphere. Perfect separation between Cherenkov and scintillation light is implemented in this simulation by using only Cherenkov photons. *Top left:* S_0 versus S_1 scatter plot. Black dotted line is a linear fit of the 90° topology and ^8B events. Variable S_{01} is defined as a projection of 2D distribution onto this linear fit. *Top right:* S_2 versus S_3 scatter plot. *Bottom:* S_{01} distributions for the three topologies. These distributions are normalized to unit area for shape comparison.

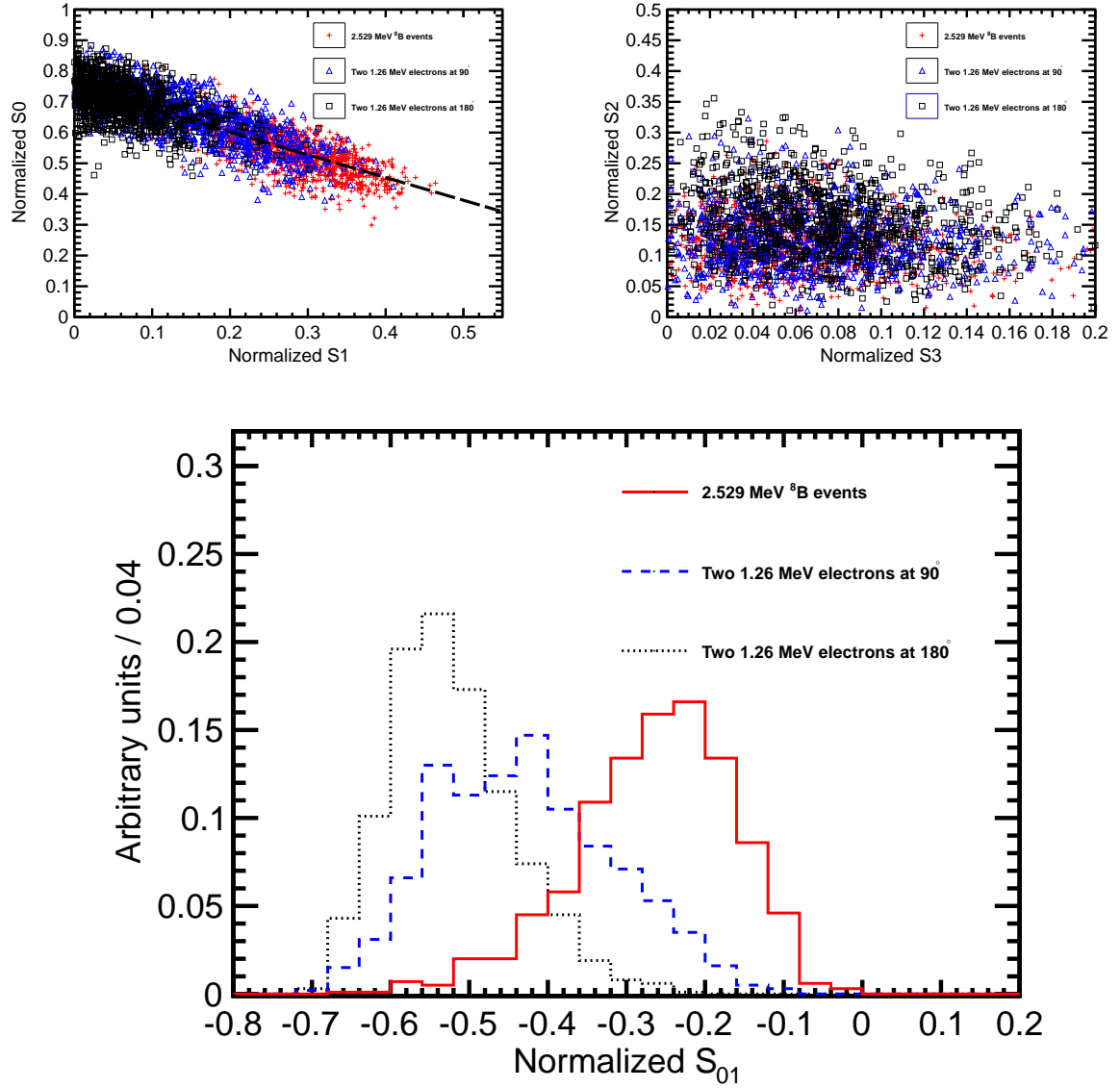


Figure 11: Spherical harmonics for three event topologies: two back-to-back 1.26 MeV electrons (*black squares and black dotted line*), two 1.26 MeV electrons at 90° angle (*blue triangles and blue dashed line*), and a single 2.529 MeV electron representing ^8B background (*red crosses and red solid line*). Simulation of 1000 events originated at the center of the sphere. Separation between Cherenkov and scintillation light is implemented 33.5 ns cut on the photon arrival time. Perfect vertex reconstruction - true vertex position is used. *Top left*: S_0 versus S_1 scatter plot. Black dotted line is a linear fit of the 90° topology and ^8B events. Variable S_{01} is defined as a projection of 2D distribution onto this linear fit. *Top right*: S_2 versus S_3 scatter plot. *Bottom*: S_{01} distributions for the three topologies. These distributions are normalized to unit area for shape comparison

4. Performance and Experimental Challenges

4.1. Performance of the spherical harmonics analysis on $0\nu\beta\beta$ decay and ^8B events.

Comparison of S_0 and S_1 distributions between $0\nu\beta\beta$ decay and ^8B events is shown in Fig. 12. There is a noticeable separation between the signal and background. We also note that in the energy range of interest S_l 's do not have strong dependence on the energy deposited in the detector, which makes them reliable discriminators at the end point of the $0\nu\beta\beta$ decay energy spectrum. The information about the event topology is complimentary to the energy measurements.

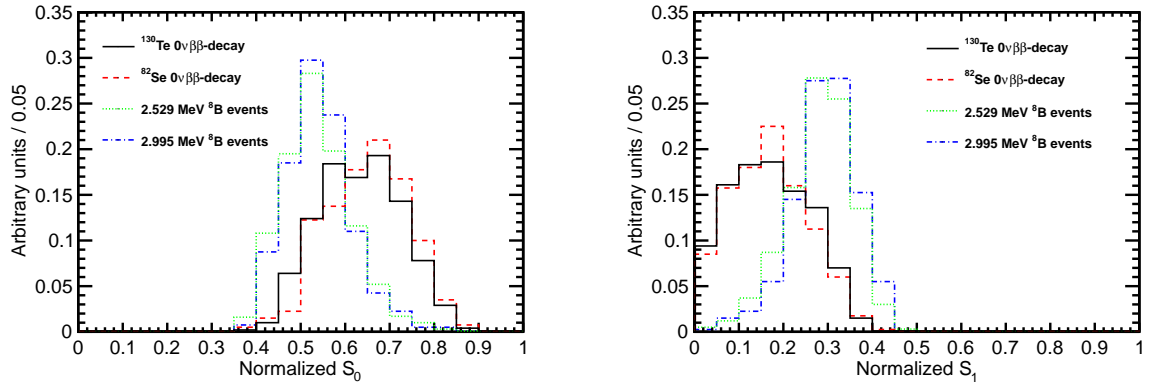


Figure 12: S_0 (left) and S_1 (right) distributions for events with two different event topologies and total kinetic energy. ^{130}Te , ^{82}Se $0\nu\beta\beta$ decay, 2.529 MeV and 2.995 MeV events are compared. The simulation is done for events with the vertex in the center of the detector. ^8B events are implemented as 2.529 MeV or 2.995 MeV electrons with initial direction along x -axis. Perfect vertex reconstruction - true vertex position is used. Time cut of 33.5 ns on the photon arrival time is applied.

Figure 13 shows separation between ^{130}Te signal and ^8B background events simulated at the center of the detector. True values of vertex position and time is used. Time cut of 33.5 ns on the photon arrival time is applied to separate Cherenkov and scintillation light. Most of the discrimination between signal and background comes from S_0 and S_1 . In the following S_2 and S_3 are not used to separate ^{130}Te and ^8B events². The scatter plot of S_2 vs S_3 is shown here for completeness.

In order to optimize separation between ^{130}Te signal and ^8B background a linear combination of S_0 and S_1 , S_{01} , is used. A linear fit, $S_0 = A \times S_1 + B$, of 2-dimensional S_0 vs S_1 scatter plot is performed as shown in Fig. 13. Then this 2-dimensional distribution is projected onto the fitted line. **A little bit of math here to quantitatively describe S_{01} via S_0 and S_1 :** A new coordinate frame is obtained by rotation of the original S_0 - S_1 frame at angle θ obtained from the fit: $\tan(\theta)=A$. A transformation, $S_{01} = S_1 \cdot \cos(\theta) + S_0 \cdot \sin(\theta)$, defines the S_{01} variable.

Bottom plot in Fig. 13 shows performance of the S_{01} variable to separate ^{130}Te signal and ^8B background. A fit to this distribution can be done to optimize the discrimination power in a particular experimental settings. Here we refrain from quantitative estimates on the improvements in sensitivity to $0\nu\beta\beta$ decay search using this method of spherical harmonics as a reliable estimate would require a dedicated analysis taking into account all the details of a particular experiment.

² S_2 and S_3 are helpful for separation of ^{130}Te signal from ^{10}C background. See Appendix.

4.2. Experimental challenges

So far only events at the center of the detector have been considered. In this section we discuss performance of the spherical harmonics analysis for events distributed within the fiducial volume of the detector taking into account finite resolution on vertex position reconstruction.

When the vertex is not at the center, a uniform time cut on the photon arrival time is no longer effective in the selection of Cherenkov photons. In the case of off-center vertex, even significantly delayed scintillation photons can reach the side of the detector that is closer to the vertex much earlier than Cherenkov photons traveling to the opposite side of the detector. Therefore, the time cut has to be position dependent and take into account the total distance traveled by each individual photon.

We found that the time cut defined as $\Delta t = t_{measured}^{phot} - t_{predicted}^{phot} < 1$ ns selects photons with sufficient fraction of Cherenkov photons. Predicted time, $t_{predicted}^{phot} = l/v^{phot}$, depends on total distance, l , traveled by the photon and proper assignment of the velocity for each photon, v^{phot} , that depends on index of refraction, (Note, we use average index of refraction of $n=1.53$). Therefore the relative Cherenkov/scintillation composition of the light selected with this Δt time cut depends on the vertex location and chromatic dispersions.

Due to chromatic dispersion, even with perfect vertex reconstruction one cannot achieve the same level of separation between Cherenkov and scintillation light compared to the central events considered above in Section 4. This in turn reduces the effectiveness of the spherical harmonics analysis in separating of $0\nu\beta\beta$ decay and ^8B events (see Fig. 14). However next generation detectors can recover losses due to chromatic dispersion by choosing liquid scintillators with a more narrow emission spectrum.

Imprecise knowledge of the vertex position due to finite resolution is another factor affecting performance of the spherical harmonics analysis. Small deviations in vertex reconstruction cause large effect on S_0 and S_1 for single electron event topology. For the vertices shifted along the direction of the electron the Δt cut makes uniform scintillation light distribution less uniform. The Δt cut selects more forward emitted photons in the case when the reconstructed vertex is shifted to the direction opposite to the electron momentum (enhancing forward region populated by Cherenkov photons - more asymmetric photon distribution causing higher values of S_1). It selects more backward emitted photons in the case when the reconstructed vertex is shifted in the direction along the electron momentum (counter balancing forward region populated by Cherenkov photons - more symmetric photon distribution causing smaller values of S_1).

Solution to this problem would be a better selection criteria of early light. It has to preserve high admixture of the Cherenkov photons, but needs to select scintillation photons in a more uniform manner. Working on it, but may not be simple so I don't want to include it in this paper.

Good vertex resolution is essential for spherical harmonics analysis. Such strong dependence on the vertex resolution can be addressed by choosing a different liquid scintillator mixture with a more delayed emission of the scintillation light. Figure ?? shows spherical harmonics calculated for the time profile which has scintillation component delayed by 0.5ns with respect to what is shown in Fig. ??

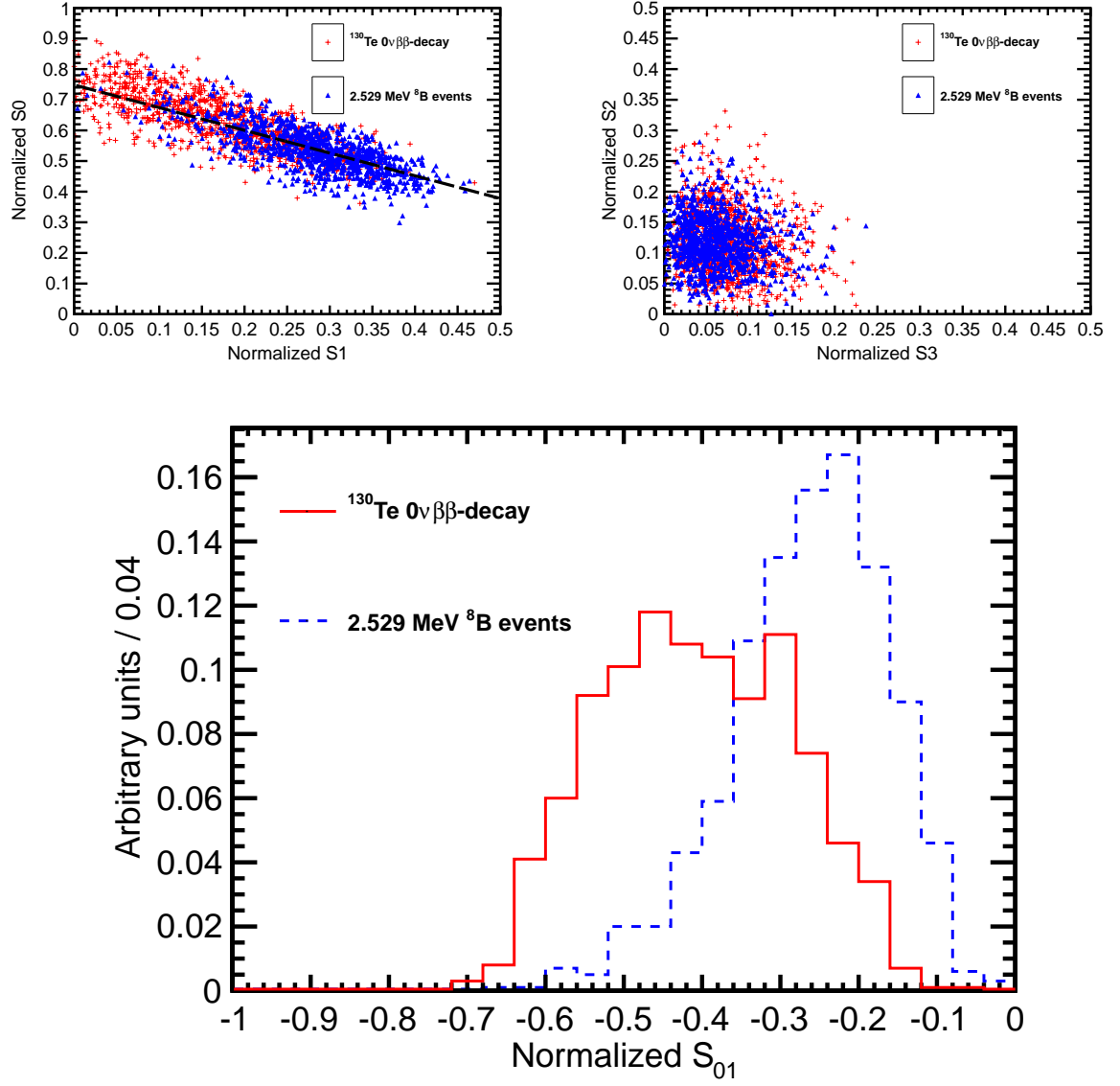


Figure 13: Spherical harmonics comparison between $^{130}\text{Te } 0\nu\beta\beta$ decay signal ($Q = 2.529$ MeV) (red) and ^8B solar neutrinos background (blue) for 1000 simulated events originated at the center of the sphere. ^8B events are implemented as 2.529 MeV electrons with initial direction along x -axis. Perfect vertex reconstruction - true vertex position is used. Time cut of 33.5 ns on the photon arrival time is applied. *Top left:* S_0 versus S_1 scatter plot. Black dotted line is a linear fit of these 2D histograms. Variable S_{01} is defined as a projection of 2D distribution onto this linear fit. *Top right:* S_2 versus S_3 scatter plot. *Bottom:* S_{01} distribution for the signal and background.

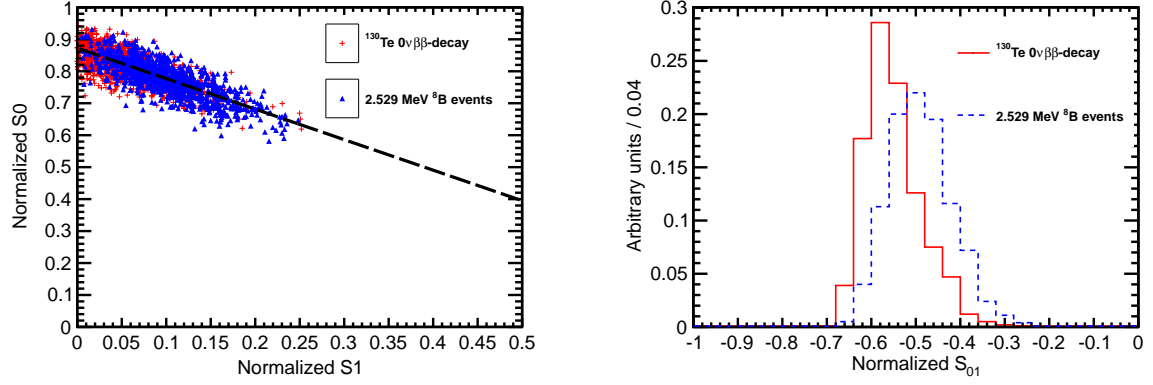


Figure 14: Spherical harmonics comparison between ^{130}Te $0\nu\beta\beta$ decay signal ($Q = 2.529$ MeV) (red) and ^8B solar neutrinos background (blue) for 1000 simulated events. Vertices are uniformly distributed within the fiducial volume, $R < 3$ m. ^8Be events are implemented as 2.529 MeV electrons with the initial momentum direction uniformly distributed within 4π solid angle. Perfect vertex reconstruction - true vertex position is used. *Left:* S_0 versus S_1 scatter plot. Black dotted line is a linear fit of these 2D histograms. Variable S_{01} is defined as a projection of 2D distribution onto this linear fit. *Right:* S_{01}

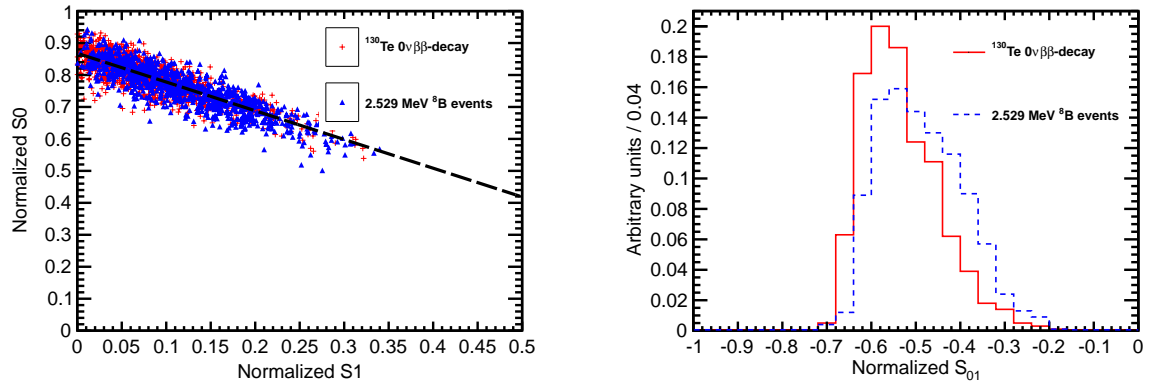


Figure 15: Spherical harmonics comparison between ^{130}Te $0\nu\beta\beta$ decay signal ($Q = 2.529$ MeV) (red) and ^8B solar neutrinos background (blue) for 1000 simulated events. Vertices are uniformly distributed within the fiducial volume, $R < 3$ m. ^8Be events are implemented as 2.529 MeV electrons with the initial momentum direction uniformly distributed within 4π solid angle. Vertex is smeared with 3 cm resolution. *Left:* S_0 versus S_1 scatter plot. Black dotted line is a linear fit of these 2D histograms. Variable S_{01} is defined as a projection of 2D distribution onto this linear fit. *Right:* S_{01}

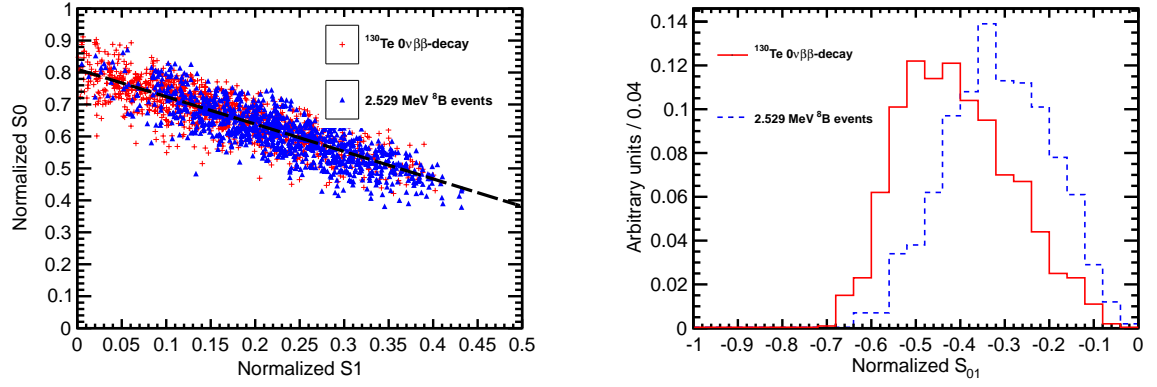


Figure 16: Spherical harmonics comparison between $^{130}\text{Te } 0\nu\beta\beta$ decay signal ($Q = 2.529$ MeV) (red) and ^8B solar neutrinos background (blue) for 1000 simulated events. Vertices are uniformly distributed within the fiducial volume, $R < 3$ m. ^8Be events are implemented as 2.529 MeV electrons with the initial momentum direction uniformly distributed within 4π solid angle. Vetrex is smeared with 3 cm resolution. **Scintillation light is delayed by additional 0.5 ns.** Left: S_0 versus S_1 scatter plot. Black dotted line is a linear fit of these 2D histograms. Variable S_{01} is defined as a projection of 2D distribution onto this linear fit. Right: S_{01}

5. Conclusions

A technique based on spherical harmonics analysis is discussed to separate $0\nu\beta\beta$ decay from ^8B solar neutrino interactions. The separation is based on distinct event topologies of signal and background. This event topology information is available in addition to the measurements of the energy deposited in the detector. This technique may be further developed and adopted by future large scale liquid scintillator detectors to suppress background coming from ^8B solar neutrino interactions in the detector volume. The performance of the technique is mostly affected by chromatic dispersions, vertex reconstruction and time profile of the emission of the scintillation light. We show that a liquid scintillator detector with a ~ 1 ns total delay of the scintillation light with respect to the Cherenkov light allows for use of spherical harmonics analysis as an extra handle to extract $0\nu\beta\beta$ decay signal.

Acknowledgements

Here are people to acknowledge.

References

A. $0\nu\beta\beta$ decay vs ^{10}C background

Other common backgrounds to $0\nu\beta\beta$ decay search include radioactive decays of nuclei excited by cosmic muons and decays of Th and U naturally present in the materials. In a liquid scintillator detectors most of events from Th and U decays are happening in the materials of the scintillator enclosure. Typically they enter the fiducial volume as 2.6 MeV gammas. These gammas either shower too late or have mis-reconstructed vertex. Both effects depend on details of a particular experiment and therefore in this paper we make no attempt to introduce a topology reconstruction for the backgrounds coming from Th and U lines. Cosmic induced backgrounds, to the contrary, are more generic and originate inside the fiducial volume. In this section we discuss event topology of ^{10}C events that are most relevant in the energy of 2-3 MeV.

Typical energy deposition by ^{10}C events is shown in Fig. A.17. We propose to use spherical harmonics analysis to separate $0\nu\beta\beta$ decay events from ^{10}C events that within energy resolution overlap with the $0\nu\beta\beta$ decay Q-value.

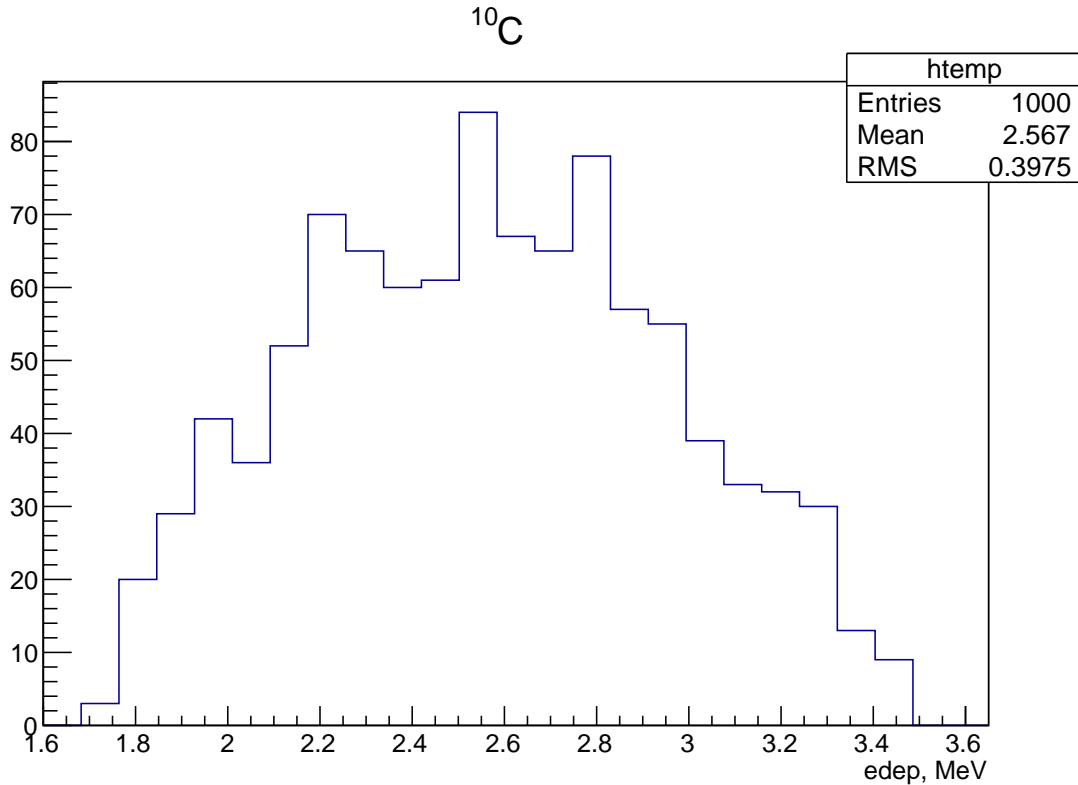


Figure A.17: Energy deposition in ^{10}C events.

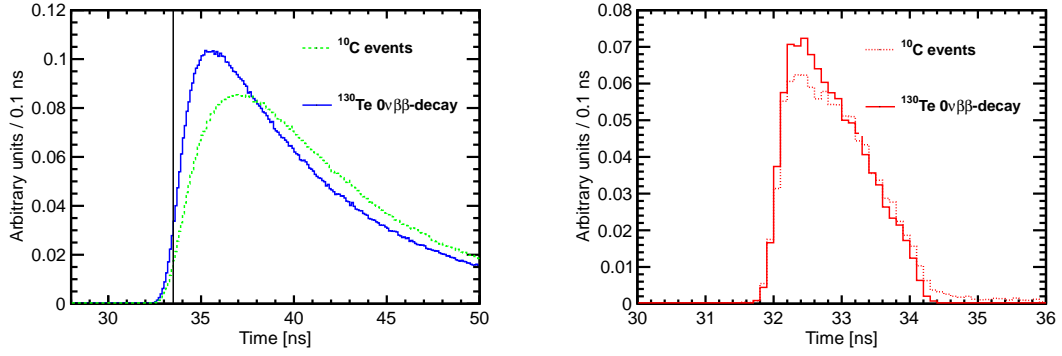


Figure A.18: Photo-electron (PE) arrival times after application of the photo-detector transit time spread (TTS) of 100 ps for the simulation of 1000 $0\nu\beta\beta$ decay events of ^{130}Te (solid lines) and ^{10}C (dotted lines) events at the center of the detector. All distributions are normalized for shape comparison. **Absolute number of PEs per event depends on the total energy deposited in the detector. Figure A.17 shows energy deposited in the detector in ^{10}C events.** *Left:* Scintillation PEs arrival time. The black vertical line illustrates a time cut at 33.5 ns. *Right:* Cherenkov PEs arrival time.

We note that 98% of ^{10}C decays through the excited state of $^{10}\text{B}(718)$ that has a half-life time of ~ 1 ns. Therefore majority of ^{10}C events have a prompt positron accompanied by a delayed 0.718 MeV gamma. This delayed gamma affects PEs arrival time distribution. Figure A.18 shows shape comparison of PEs arrival time distribution between ^{130}Te $0\nu\beta\beta$ decay and ^{10}C events. Time profile of the scintillation photons can be used to separate signal from ^{10}C events.

Comparison of spherical harmonics is shown in Fig. A.19. ^{10}C events are generated at the center of the detector. True vertex position is used to apply a 33.5 ns time cut to select photons for the spherical harmonics analysis. The separation is seen in S0 vs S1 and S2 vs S3 scatter plots. We project both scatter plots to a line that gives maximum separation (two bottom panels in Fig. A.19).

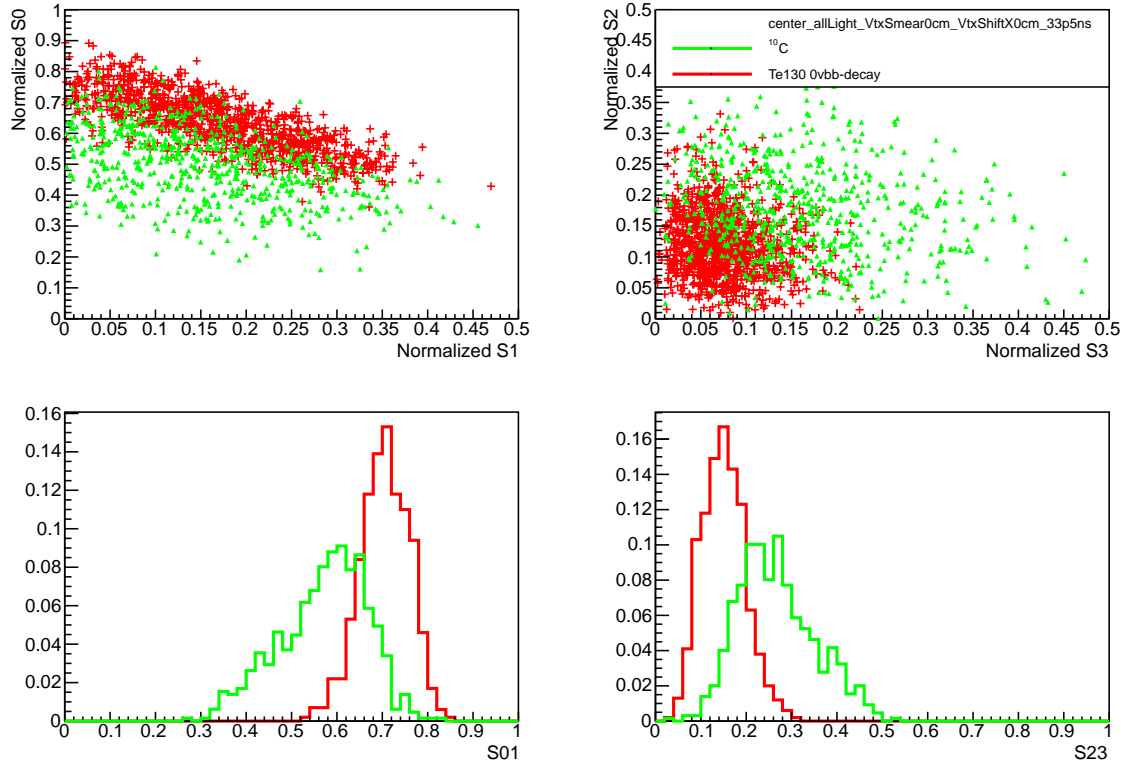


Figure A.19: Spherical harmonics comparison between ^{130}Te $0\nu\beta\beta$ decay signal ($Q = 2.529$ MeV) (red) and ^{10}C solar neutrinos background (blue) for 1000 simulated events originated at the center of the sphere. ^{10}C with energy deposition between 2.1 MeV and 2.9 MeV are considered. Perfect vertex reconstruction - true vertex position is used. Time cut of 33.5 ns on the photon arrival time is applied. *Top left:* S_0 versus S_1 scatter plot. *Top right:* S_2 versus S_3 scatter plot. *Bottom left:* Distribution of the S_0^{C10} variable calculated for signal (red) and background (green). *Bottom right:* Distribution of the S_2^{C10} variable calculated for signal (red) and background (green).